Research Article

Journal of Environmental Nanotechnology

ZrO_2-FeO-Decorated N-doped rGO Nanocomposites: Synthesis and Assessment of Antimicrobial and Antioxidant Activities

S. Nivetha[1], J. Rosaline Vimala[1*], A. Devadharshini Amala[1], A. Agila[1], A. Anitha Immaculate[2] and Chinnappan Baskar[3]

[1]Department of Chemistry, Holy Cross College (Autonomous), Affiliated to Bharathidasan University, Tiruchirappalli, TN, India
[2]Department of chemistry, Emmet A. Denis college of natural sciences, Cuttington University, Suakoko, Bong County, Liberia
[3]Department of Chemistry, Central University of Kashmir, Ganderbal, J & K, India
Received: 23.07.2026 Accepted: 25.08.2026 Published: xx.xx.xxxx
*rosalinevimala@hcctrichy.ac.in

ABSTRACT

The development of multifunctional nanomaterials with combined structural and biological properties is of significant interest in nanoscience. In this study, ZrO_2–FeO@N-rGO nanocomposite was synthesized through an eco-efficient approach and characterized using UV–Vis, FT-IR, XRD, SEM, TEM, XPS, DLS, and EDX analyses. The nanocomposite exhibited an absorption maximum at 202 nm with an optical band gap of 6.14 eV. XRD confirmed the crystalline metal oxide phases and N-rGO structure, with a crystallite size of approximately 50 nm. SEM and TEM revealed well-dispersed ZrO_2 and FeO nanoparticles anchored on wrinkled N-rGO sheets. DLS showed a Z-average diameter of 208.2 nm with a PDI of 0.278. EDX confirmed Fe and Zr contents of 18.74 and 13.38 wt%, respectively, while XPS verified Zr^{4+} and Fe^{2+}/Fe^{3+} surface states. The nanocomposite exhibited concentration-dependent antioxidant activity, with maximum scavenging efficiencies of 50.70% DPPH, 68.64% H_2O_2, and 77.56% nitric oxide at 500 µg/mL. Overall, ZrO_2–FeO@N-rGO demonstrates promising structural, antioxidant, and antimicrobial properties, supporting its potential for biomedical and environmental applications.

Keywords: ZrO_2–FeO nanocomposite; Nitrogen-doped reduced graphene oxide; Metal oxide nanocomposites; Antimicrobial activity; Antioxidant activity; Biomedical nanomaterials; Multifunctional nanocomposites.

1. INTRODUCTION

Nanocomposites composed of materials integrated at the nanoscale have attracted enormous attention because of their unique physicochemical properties and wide technological applications. These materials exhibit enhanced structural, optical, catalytic, and biological characteristics compared to their bulk counterparts, making them promising candidates for applications in nanomedicine, antimicrobial systems, biosensors, environmental remediation, and advanced electronics (Anjaneyulu *et al.* 2019). In particular, bimetallic nanocomposites are nanomaterials composed of two different metal components combined at the nanoscale, forming structures such as alloys, core-shell, or hybrid systems. These materials often exhibit enhanced catalytic, electronic, and biological properties due to the synergistic interaction between the two metals. As a result, bimetallic nanocomposites generally show improved activity, stability, and functionality compared with single-metal nanomaterials (Sharma *et al.* 2019). The major advantages of bimetallic nanocomposites are illustrated in Figure 1, highlighting their improved catalytic efficiency, enhanced biological activity, and multifunctional applications in biomedical and environmental fields.

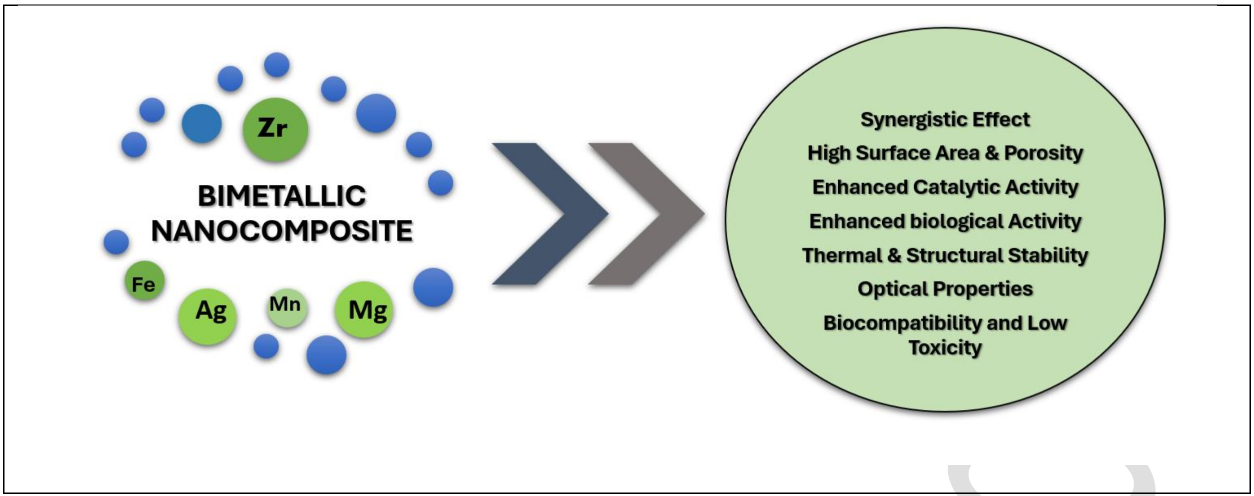

Fig. 1: Schematic representation of the advantages of bimetallic nanocomposites

Zirconium-based materials have gained increasing attention in biomedical research due to their excellent chemical stability, biocompatibility, corrosion resistance, and mechanical strength (Rane *et al*. 2018). Although zirconium itself does not possess strong intrinsic antimicrobial properties, the incorporation of zirconium oxide (ZrO_2) into nanocomposite systems has been reported to enhance the biological performance and stability of hybrid materials (Vengatesan *et al*. 2019). In particular, ZrO_2 can function as an efficient support matrix for metal nanoparticles, improving their dispersion, stability, and controlled ion release behavior (Stephanie *et al.* 2021). The antimicrobial activity of metal nanoparticles primarily arises from their ability to disrupt microbial cell membranes, interfere with intracellular metabolic pathways, and generate reactive oxygen species (ROS), ultimately leading to microbial cell death. In addition, certain metal nanoparticles can directly interact with bacterial cell walls, causing structural damage and membrane permeability, which further enhances their bactericidal effectiveness (Nagaraj *et al.* 2024).

Recent studies have shown that combining zirconium with other metal or metal-oxide nanoparticles can significantly improve antimicrobial efficiency due to synergistic interactions between the components. For instance, hybrid nanocomposites can regulate the release of metal ions, enhance surface reactivity, and improve contact with microbial cells, thereby increasing antibacterial performance (Kaliyaperumal *et al*. 2025a). The antibacterial mechanisms of such nanocomposites typically involve cell membrane disruption, oxidative stress induced by ROS generation, and inhibition of essential cellular processes such as DNA replication and protein synthesis (Kaliyaperumal *et al.* 2025b).

Recently, the development of graphene-based nanocomposites, particularly reduced graphene oxide (rGO) and nitrogen-doped reduced graphene oxide (N-rGO), has opened new opportunities for designing high-performance nanomaterials. Graphene derivatives offer large surface area, high electrical conductivity, mechanical stability, and abundant functional groups, which facilitate the effective anchoring of metal oxide nanoparticles and improve their catalytic and biological properties (Rajalakshmi *et al.* 2025). Several studies have investigated zirconium- and iron-based nanocomposites for environmental and catalytic applications, including adsorption systems and membrane materials. For example, zirconium–iron oxide nanocomposites have been reported for heavy-metal removal and water purification applications, demonstrating improved adsorption capacity and structural stability. Additionally, Fe_3O_4@ZrO_2 core–shell nanostructures and zirconium ferrite nanoparticles have been explored for membrane filtration, catalytic processes, and energy applications. However, studies focusing on graphene-supported zirconium–iron nanocomposites for biological applications remain limited, highlighting the significance of the present investigation (Mohan *et al.* 2025).

Therefore, the development of multifunctional hybrid nanocomposites incorporating ZrO_2, iron oxide, and N-rGO remains an emerging research area with significant potential (Gayathri and Balan, 2021). The incorporation of N-rGO provides enhanced surface area and electron transfer capability, while Fe-based oxides contribute magnetic and catalytic properties, and ZrO_2 improves structural stability and biocompatibility. The synergistic interaction among these components is expected to produce nanocomposites with enhanced biological performance compared to individual materials (Kumar *et al.* 2024).

In this context, the present study reports the synthesis of ZrO_2–FeO-decorated N-rGO nanocomposites and investigates their antimicrobial and antioxidant activities. The work aims to elucidate the relationship between structural characteristics, surface chemistry, and biological performance of the synthesized nanocomposite. By integrating zirconium oxide and iron oxide nanoparticles onto an N-rGO platform, the study explores the synergistic effects responsible for improved biological activity, providing valuable insights for the development of next-generation multifunctional nanomaterials for biomedical applications (Devendran and Lakshmi, 2025).

To further highlight the novelty of the present work, a comparative analysis with previously reported zirconium- and iron-based nanocomposites is presented in Table 1, demonstrating the distinct features and advantages of the synthesized ZrO_2–FeO@N-rGO system.

Table 1. Comparison of previously reported zirconium/iron-based nanocomposites with the present ZrO_2–FeO@N-rGO nanocomposite

Material System	Synthesis Method	Application Investigated	Ref.
Zirconium–iron oxide nanocomposite	Chemical synthesis	Adsorption of antimony ions from water. Focus limited to environmental remediation	(Liu *et al.* 2021)
Magnetic chitosan–ZrO_2–Fe_3O_4 nanocomposite	Hydrothermal/chemical method	Removal of Cr(VI) ions from wastewater; designed mainly for adsorption	(Korde *et al.* 2022)
Fe_3O_4@ZrO_2 core–shell nanocomposite	Sol–gel method	Membrane filtration and antifouling	(Noormohamadi *et al.* 2017)
Zirconium ferrite nanoparticles	Hydrothermal synthesis	Energy and catalytic applications	(Sahoo *et al.* 2025)
ZrO_2/ZnO/TiO_2 nanocomposite coating	Chemical deposition	• Antibacterial surface coating	(Lee *et al.* 2022)

Novelty of Present Study (ZrO_2–FeO@N-rGO)

- ZrO_2–FeO decorated N-rGO nanocomposite
- Controlled chemical synthesis with N-doped graphene integration
- Present work integrates ZrO_2–FeO with N-rGO, improving surface functionality and enabling biological applications such as Antimicrobial activity and Antioxidant activity.

2. METHODOLOGY

2.1 Reagents

Zirconium oxychloride octahydrate ($ZrOCl_2 \cdot 8H_2O$), ferric chloride hexahydrate ($FeCl_3 \cdot 6H_2O$), and sodium hydroxide (NaOH) were used as precursor materials for the synthesis of the bimetallic nanocomposite. Graphite powder served as the precursor for graphene oxide (GO) synthesis. Ammonium hydroxide (NH_4OH) was used as the nitrogen source for nitrogen doping. Concentrated sulfuric acid (H_2SO_4) and potassium permanganate ($KMnO_4$) were used in the modified Hummers' method for graphene oxide preparation. Deionized water was used throughout all experimental procedures to minimize contamination. For biological assay, A. israelii-1303 was purchased from ATCC. (*P.Vulgaris-426) and (Candida Albicans, Trichoderma*) were purchased from MTCC, Chandigarh, India. HEK-293 (Human Embryonic Kidney cells) and A549 (Human Lung Cancer cells) cell lines were purchased from NCCS, Pune. All reagents were purchased from commercial suppliers and used without further purification unless otherwise stated.

2.2 Synthesis of Nitrogen-doped Reduced Graphene Oxide (N-rGO)

Graphene oxide (GO) was first synthesized from graphite powder using a modified Hummers' method. In this process, graphite was oxidized using concentrated sulfuric acid and potassium permanganate under controlled conditions, followed by repeated washing and exfoliation to obtain GO (Yang *et al.* 2017). The obtained GO was dispersed in deionized water by ultrasonication for 30 min to form a homogeneous suspension. Ammonium hydroxide was then added as the nitrogen source. The mixture was transferred into a Teflon-lined stainless-steel autoclave and subjected to hydrothermal treatment at 180°C for 12 h. During this process, simultaneous reduction of GO and nitrogen doping occurred, resulting in the formation of nitrogen-doped reduced graphene oxide (N-rGO). The product was collected by centrifugation, washed several times with deionized water and ethanol to remove residual impurities, and dried at 60°C for 12 h (Sanmugam *et al.* 2024; Agarwal and Zetterlund, 2021). The schematic representation of the synthesis procedure of N-rGO is illustrated in Fig. 2.

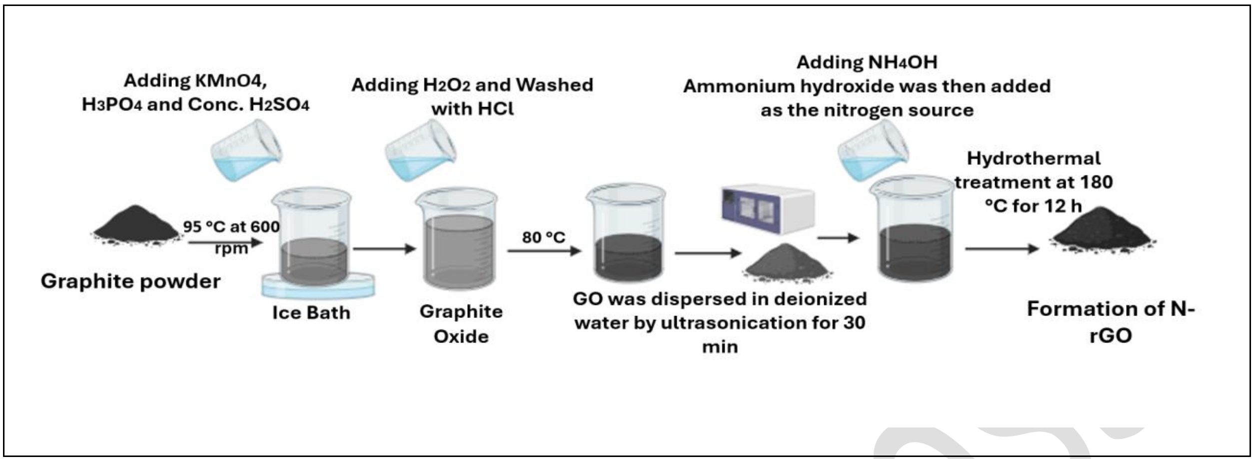

Fig. 2: Schematic illustration of the synthesis process of nitrogen-doped reduced graphene oxide (N-rGO)

2.3 Synthesis of ZrO_2–FeO@N-rGO Nanocomposite

For the fabrication of the ZrO_2–FeO@N-rGO nanocomposite, 0.2 g of N-rGO was dispersed in 100 mL of deionized water using ultrasonication for 30 min to obtain a stable suspension. Subsequently, 0.1 M zirconium oxychloride and ferric chloride solutions were added dropwise to the N-rGO dispersion under continuous stirring to promote adsorption of metal ions onto the graphene sheets. Rutin dissolved in 10 mL of ethanol was then introduced slowly into the reaction mixture. Co-precipitation was induced by gradually adding 1 M NaOH until the pH reached 9–11, enabling the simultaneous formation and deposition of ZrO_2 and FeO nanoparticles on the N-rGO surface. The reaction mixture was stirred continuously for 4 h at room temperature, followed by mild heating at 60–80°C to enhance nanocomposite formation (Águila-Martínez *et al.* 2025). The final product was collected by centrifugation, washed several times with deionized water and ethanol to remove unreacted species, and vacuum-dried at 50°C to obtain the ZrO_2–FeO@N-rGO nanocomposite (Arayesh *et al.* 2023). All experiments were performed in triplicate to ensure reproducibility. The schematic representation of the synthesis procedure of ZrO_2–FeO@N-rGO nanocomposite is illustrated in Fig. 3.

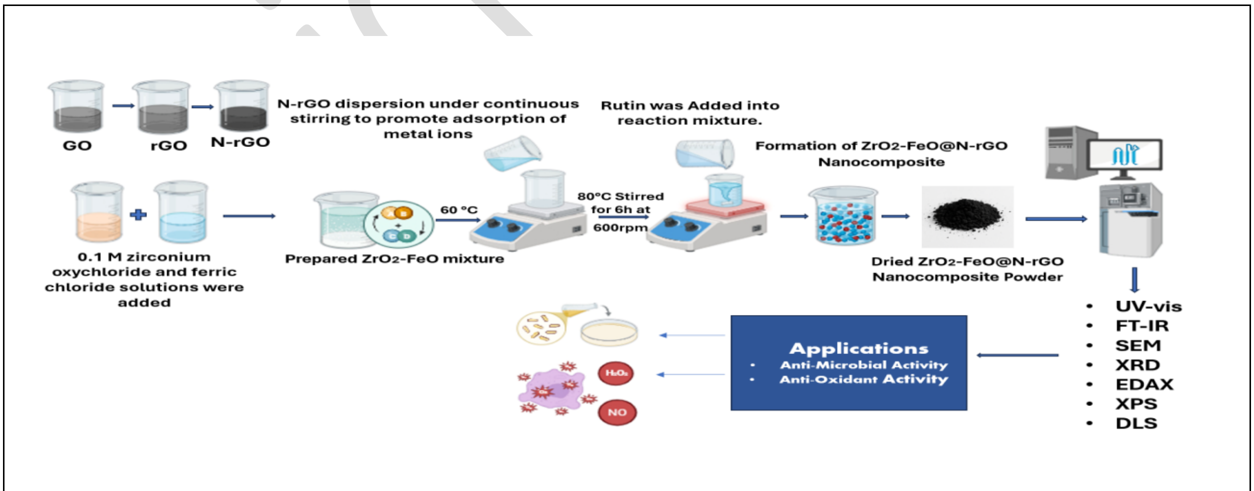

Fig. 3: Schematic illustration of the synthesis process of ZrO_2–FeO@N-rGO nanocomposite

2.4 Characterization Techniques

A comprehensive set of characterization techniques was employed to evaluate the structural, chemical, and optical attributes of the ZrO_2–FeO@N-rGO nanocomposite. Scanning electron microscopy (SEM, CAREL ZEISS EVO 18) was used to examine surface morphology. Crystalline phases and structural integrity are confirmed by X-ray diffraction (XRD). Fourier-transform infrared spectroscopy (FT-IR, Perkin

Elmer Spectrum Two, 4000–400 cm^{-1}) provides information on functional groups and bonding interactions within the composite, while energy-dispersive X-ray spectroscopy (EDX) validates the elemental composition and confirms the effective nitrogen incorporation into the rGO framework. UV–Vis spectroscopy (Perkin Elmer Lambda 35, 190–1100 nm) was employed to assess the optical response and to identify characteristic absorption signatures associated with rutin and N-rGO. Dynamic light scattering (DLS, Micromeritics Nano Plus) was used to determine hydrodynamic particle size and dispersion stability, offering insight into the colloidal behavior of the nanocomposite. Collectively, these complementary characterization techniques furnish a detailed understanding of the composite's structure, composition, and functional performance, supporting its potential for biomedical and advanced technological applications Shaba *et al.* (2024).

2.5 Biomedical Activity Assessment

The biological performance of the synthesized nanocomposites was examined through a series of antimicrobial and antioxidant assays. Antibacterial and antifungal activities were assessed using standard *in vitro* diffusion-based methods. For antibacterial evaluation, agar well diffusion and disc diffusion techniques were conducted on nutrient agar plates inoculated with representative bacterial species, including *Proteus vulgaris* and *Actinomyces israelii*. Following treatment with different concentrations of the nanocomposites, inhibition zones formed around the disc were measured to quantify antibacterial effectiveness. Antifungal activity was evaluated on potato dextrose agar plates seeded with fungal strains such as *Candida albicans* and *Trichoderma* spp., where the diameter of inhibition zones served as an indicator of antifungal potential (Gautam *et al.* 2024). Gentamicin and amphotericin B were used as positive controls to ensure method validity and comparative assessment. The antioxidant activity of the synthesized ZrO_2–FeO@N-rGO nanocomposite was evaluated using DPPH, hydrogen peroxide, and nitric oxide radical scavenging assays. The percentage of radical scavenging activity was calculated using the following equation: (Madhuranga and Samarakoon, 2023).

$$\% \text{ Inhibition} = {(Ac - As)}/{\text{Ac}} \times 100$$

where *Ac* represents the absorbance of the control and *As* represents the absorbance of the sample. This equation was used to determine the ability of the nanocomposite to neutralize free radicals by comparing the absorbance of the control solution with that of the sample-containing solution. The same calculation method was applied for DPPH, H_2O_2, and nitric oxide scavenging assays to estimate the antioxidant potential of the nanocomposite. This method is widely used for evaluating antioxidant activity in nanomaterial-based systems to monitor the material's ability to scavenge free radicals and mitigate oxidative stress. (Munteanu and Apetrei, 2021).

2.6 Standard Methods Used for Biological Assays

The experimental procedures employed in this study were conducted in accordance with established national and international guidelines to ensure reliability and reproducibility. Antimicrobial activity was evaluated using the agar diffusion method following the Clinical and Laboratory Standards Institute (CLSI) guidelines (CLSI M02 and CLSI M100). Antifungal susceptibility testing was performed according to CLSI M27 standards. The Antimicrobial activity values were calculated using Graph Pad Prism 6.0 Software (USA). Particle size measurements using dynamic light scattering (DLS) were carried out following ISO 22412:2017 standards for nanoparticle size analysis. Additionally, antioxidant activity was determined using the DPPH radical scavenging assay according to widely accepted IUPAC-recommended protocols.

2.7 Statistical Analysis

All experiments were performed in triplicate to ensure reproducibility, and the results are expressed as mean ± standard deviation (SD). Statistical analysis was carried out using one-way analysis of variance (ANOVA) to evaluate differences between experimental groups at different concentrations. A *p*-value less than 0.05 ($p < 0.05$) was considered statistically significant. Graphical representations were prepared using standard scientific plotting tools, and error bars represent the standard deviation obtained from three independent experiments (n = 3). The calculated IC_{50} values for antioxidant assays were obtained from the concentration–response curves.

3. RESULTS AND DISCUSSION

3.1 UV–Visible Spectroscopy Analysis

Figure 4 presents the UV–Vis absorption spectra of ZrO_2, FeO, and the ZrO_2–FeO@N-rGO nanocomposite, highlighting their distinct optical responses. ZrO_2 shows a sharp absorption peak at around 202 nm, assigned to $O^{2-} \rightarrow Zr^{4+}$ ligand-to-metal charge transfer typical of wide band gap zirconia, consistent with earlier reports on rGO-supported ZrO_2 systems (Soltanpour *et al.* 2024). FeO exhibits a broader band centered near 247 nm, characteristic of overlapping d–d transitions of Fe^{2+}/Fe^{3+} and commonly observed in iron-rich oxides with multiple electronic pathways and extended UV–visible absorption (Potbhare *et al.* 2024). The ZrO_2–FeO@N-rGO nanocomposite displays an intense peak at about 203 nm with markedly higher absorbance than the individual oxides, indicating strong electronic coupling between ZrO_2 and FeO facilitated by the conductive N-doped rGO network, in line with studies showing that graphene-based supports enhance charge transfer and tune the optical behavior of metal oxide hybrids (Al-Gaashani *et al.* 2023).

The optical band gap energies of the synthesized samples were calculated from their UV–Vis absorption edges using the relationship Eg=1240/λE, where λ is the absorption edge wavelength in nm, a method widely employed for semiconductor oxides and their nanocomposites. The estimated band gap values for ZrO_2, FeO, and ZrO_2–FeO@N-rGO nanocomposite are approximately 6.11, 5.02, and 6.14 eV, respectively, which are consistent with earlier reports that describe ZrO_2 as a wide-band-gap semiconductor with deep-UV absorption and Fe-based oxides as relatively narrower-gap components capable of extending the photoresponse toward longer wavelengths when coupled appropriately. Previous studies on ZrO_2/Fe_2O_3 and related ZrO_2/transition-metal-oxide systems have shown that the introduction of a secondary oxide and conductive carbon phases such as rGO can markedly improve visible-light harvesting and charge separation through interfacial Zr–O–M (M = metal) and M–O–C linkages, even when the apparent band edge position remains largely unchanged, which supports the role of N-rGO here in promoting efficient electron transport and suppressing recombination in the ZrO_2–FeO@N-rGO nanocomposite. This synergistic band-structure modulation and amplified absorption suggest that the ZrO_2–FeO@N-rGO nanocomposite is a promising candidate for advanced biosensing, photocatalytic, and optoelectronic applications.

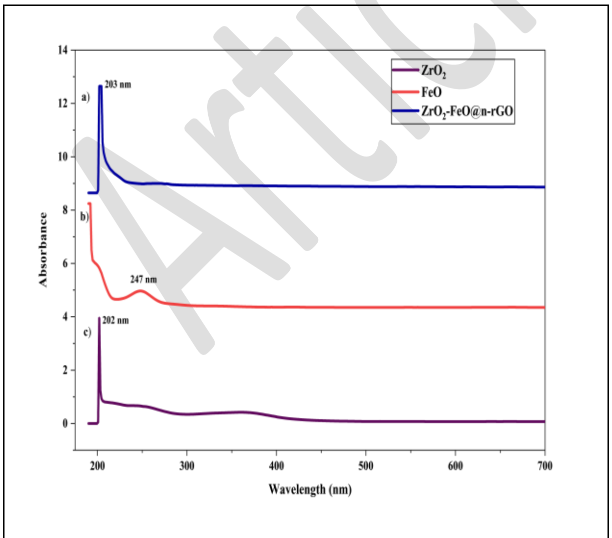

Fig. 4: UV-visible absorption spectra of (a) ZrO_2, (b) FeO, and (c) ZrO_2-FeO@N-rGO nanocomposite

3.2 FT-IR Spectrum Spectroscopy Analysis

The FT-IR spectra of ZrO_2, FeO, and the ZrO_2–FeO@N-rGO nanocomposite are shown in Figure 5, which reveals the key functional groups and bonding interactions. ZrO_2, FeO, and the ZrO_2–FeO@N-rGO nanocomposite display a broad and intense absorption band in the range of 3434–3453 cm^{-1}, corresponding to O–H stretching vibrations from surface hydroxyl groups and adsorbed moisture, while bands near 1634–1638 cm^{-1} are attributed to H–O–H bending modes. Such hydroxyl functionalities are commonly observed in metal oxide nanomaterials synthesized via aqueous or hydrothermal methods and are known to influence surface reactivity and interfacial interactions (Mylarappa *et al*. 2024). A distinct band around 1540–1560 cm^{-1} is assigned to C=C stretching of restored sp^2 carbon domains, confirming successful reduction and nitrogen doping of graphene oxide. Similar FT-IR features have been widely reported for zirconium oxide, iron oxide, and graphene-based nanocomposites and are associated with enhanced surface polarity and biological compatibility.

Characteristic metal–oxygen stretching vibrations appear in the low-wavenumber region, with bands at ~711 cm^{-1} (Zr–O) and ~688 cm^{-1} (Fe–O). In the composite, a shifted band at ~661 cm^{-1} suggests strong interfacial interactions between ZrO_2 and FeO nanoparticles anchored on the N-rGO framework. Weak features in the 2075–2113 cm^{-1} region further support the presence of C–N-related functionalities. Such peak shifts are indicative of composite formation and lattice distortion caused by metal–metal and metal–support interactions (Thamer *et al.* 2024). The presence of these bands supports the formation of metal–O–C and metal–O–N linkages, which facilitate charge transfer and enhance structural stability, as reported for other N-rGO-based metal oxide nanocomposites (Mustafa *et al.* 2023). These results confirm effective hybridization and composite formation.

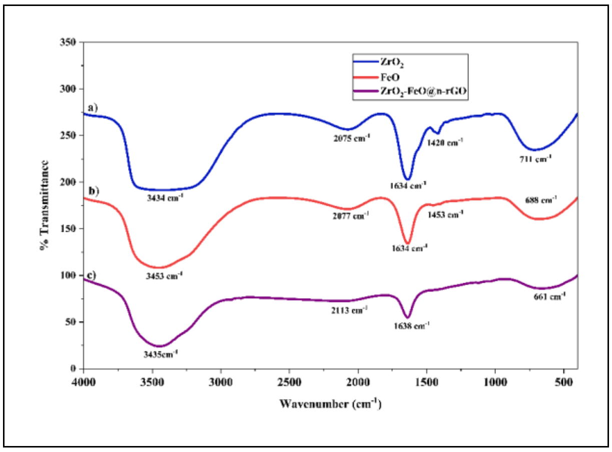

Fig. 5: FT-IR spectra showing functional groups present in (a) ZrO_2, (b) FeO and (c) ZrO_2-FeO@N-rGO nanocomposite

3.3 Scanning Electron Microscope

The surface morphology and particle distribution of the synthesized ZrO_2, FeO, and ZrO_2–FeO@N-rGO nanocomposite were examined using scanning electron microscopy, as illustrated in Figure 6. Figure 6a shows the SEM image of ZrO_2 nanoparticles, which exhibit relatively uniform, dense, and compact particulate structures with smooth surfaces and well-defined crystalline facets. Although partial aggregation is observed, the individual particles remain distinguishable, indicating well-developed nanoscale domains. The average particle size of ZrO_2 is estimated to be in the range of 40–60 nm, which is consistent with recent reports on solution-processed ZrO_2 nanoparticles exhibiting faceted morphologies and narrow size distributions (Sanjeevarayappa *et al.* 2024).

Figure 6b presents the SEM image of FeO nanoparticles, revealing a distinct fibrous and flaky morphology composed of elongated nanosheets and rod-like structures. This anisotropic morphology reflects different crystal growth dynamics and comparatively loose packing, resulting in increased surface area. Similar fibrous and aggregated morphologies have been reported for iron oxide nanostructures synthesized via wet-chemical routes, where Fe^{2+}/Fe^{3+} redox behavior influences particle growth and aggregation (Al-Ansari *et al.* 2024)

The SEM image of the ZrO_2–FeO@N-rGO nanocomposite (Figure 6c) demonstrates a heterogeneous hybrid architecture in which compact ZrO_2 nanoparticles and fibrous FeO nanostructures are uniformly anchored onto wrinkled and layered nitrogen-doped reduced graphene oxide sheets. The embedded nanoparticles exhibit an average size distribution, indicating that the presence of the N-rGO matrix effectively suppresses excessive particle growth and minimizes agglomeration. Similar morphology control and improved dispersion have been reported for metal oxide–graphene-based nanocomposites, where graphene sheets act as conductive scaffolds and physical barriers, enhancing interfacial contact and electron transport (Hussein *et al.* 2025). Overall, the observed morphology confirms the successful integration of ZrO_2 and FeO within the N-rGO framework.

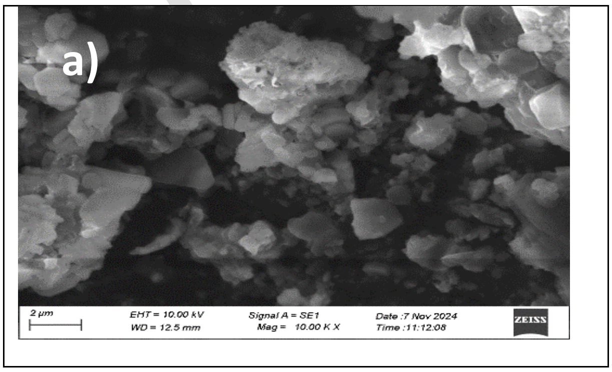

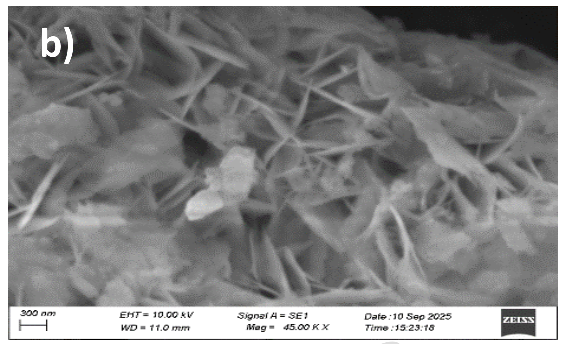

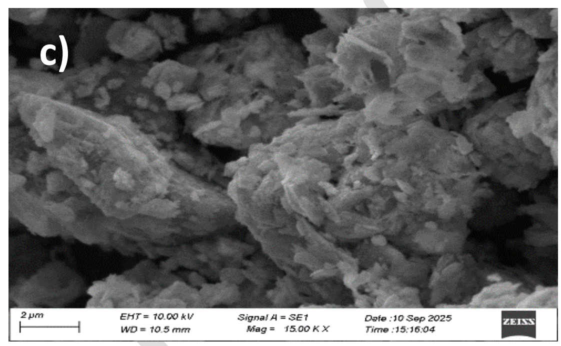

Fig. 6: SEM micrographs illustrating the surface morphology of (a) ZrO_2, (b) FeO and (c) ZrO_2-FeO@N-rGO nanocomposite

3.3.1 Transmission Electron Microscopy

Figure 7 shows that the transmission electron microscopy (TEM) analysis confirms the successful synthesis of the ZrO_2–FeO@N-rGO nanocomposite with a well-integrated heterostructured morphology. The low-magnification TEM images reveal thin, wrinkled, and transparent N-doped reduced graphene oxide (N-rGO) sheets uniformly decorated with rod-like and irregularly shaped ZrO_2 and FeO nanoparticles, indicating effective immobilization of the metal oxides on the graphene support while minimizing particle agglomeration. The nanoparticles are homogeneously distributed throughout the graphene matrix, forming an interconnected porous architecture that provides abundant active sites and facilitates efficient electron transport. High-resolution TEM (HRTEM) images exhibit well-defined lattice fringes, confirming the high crystallinity of the embedded metal oxide nanoparticles and the formation of intimate interfacial contact between ZrO_2, FeO, and the N-rGO support. Furthermore, the selected area electron diffraction (SAED) patterns display distinct concentric diffraction rings with bright diffraction spots, characteristic of a polycrystalline structure, which verifies the coexistence of crystalline ZrO_2 and FeO phases within the composite. The strong oxide–graphene interaction, uniform nanoparticle dispersion, and hierarchical porous morphology collectively demonstrate the successful fabrication of the ZrO_2–FeO@N-rGO nanocomposite, which is expected to enhance charge transfer kinetics, increase the density of accessible active sites, and improve the overall catalytic and electrochemical performance of the material.

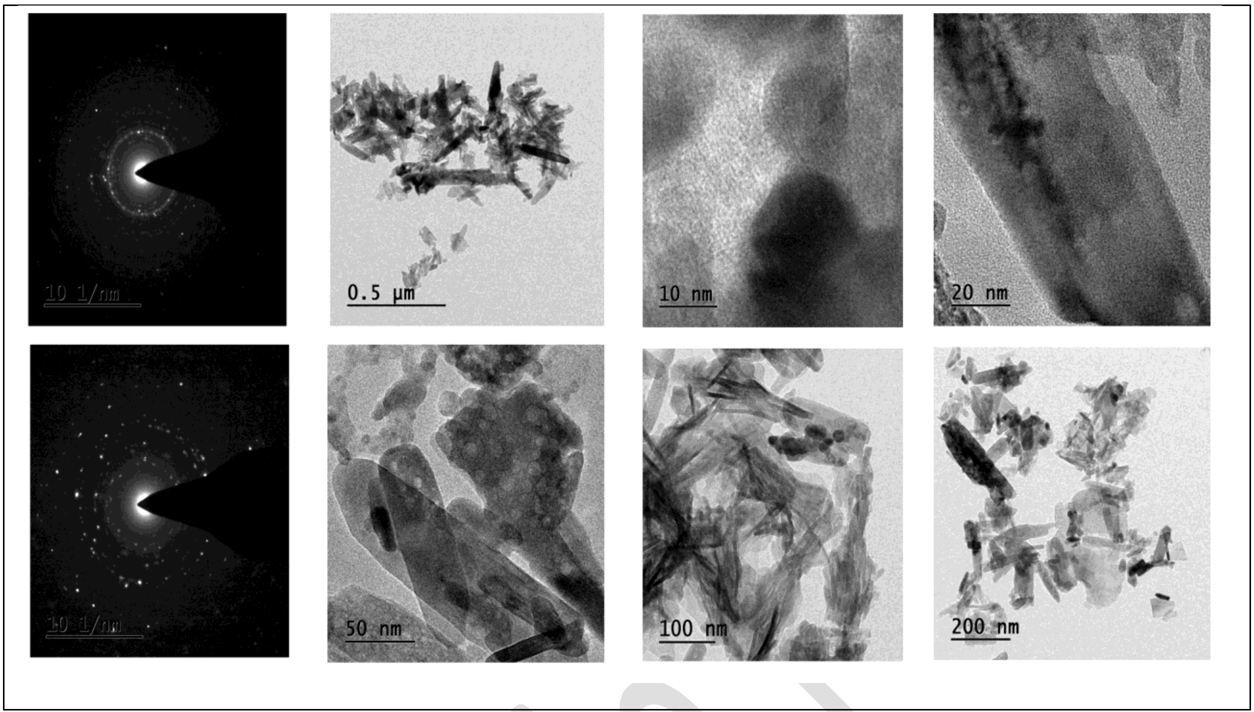

Fig. 7: Transmission electron microscopy (TEM) characterization of the synthesized ZrO_2–FeO@N-rGO nanocomposite, including selected area electron diffraction (SAED) patterns, low- and high-magnification TEM images, and high-resolution TEM (HRTEM) images, demonstrating the homogeneous dispersion of crystalline ZrO_2 and FeO nanoparticles on wrinkled N-doped reduced graphene oxide (N-rGO) sheets

3.4 X-ray Diffraction Analysis

Figure 8 shows the XRD patterns of ZrO_2 nanoparticles, FeO nanoparticles, and the ZrO_2–FeO@N-rGO nanocomposite. The ZrO_2 sample shows broad diffraction features with peaks around $2\theta \approx 22.8°$, 40.8°, and 61.4°, indicating well-defined peaks and partially amorphous nature. In contrast, FeO exhibits sharp and intense peaks at $2\theta \approx 31.6°$, 34.3°, 36.1°, 56.5°, and 62.6°, corresponding to well-defined crystalline planes of iron oxide (JCPDS No. 19-0629). The ZrO_2–FeO@N-rGO nanocomposite displays combined diffraction peaks at $2\theta \approx 26.6°$, 32.0°, 45.7°, 56.7°, and 75.5°, confirming the successful incorporation of ZrO_2 and FeO within the N-rGO matrix. The peak at ~26° is attributed to the (002) plane of N-rGO. Compared to pure FeO, slight peak broadening and reduced intensity are observed, indicating crystallite size and improved dispersion of nanoparticles on the graphene support, which enhances surface area and functional activity. The diffraction pattern of ZrO_2 nanoparticles exhibits sharp and well-defined peaks corresponding to the characteristic crystallographic planes of tetragonal and monoclinic zirconia phases, confirming the high crystallinity of the synthesized ZrO_2 nanoparticles. Similar diffraction features for crystalline ZrO_2 nanoparticles have been widely reported in previous studies (Nanda and Yi, 2024).

The XRD pattern of FeO nanoparticles shows intense reflections indexed to the typical crystallographic planes of iron oxide, indicating good phase purity and well-defined crystallite structure. Such ROS generation is one of the key mechanisms responsible for the antimicrobial and antioxidant behavior of metal oxide nanomaterials (Elshypany *et al.* 2021). For the ZrO_2–FeO@N-rGO nanocomposite, the XRD profile displays diffraction peaks corresponding to both ZrO_2 and FeO phases, confirming the successful incorporation of both metal oxides within the composite structure.

The crystallite sizes were calculated using the Debye–Scherrer equation, yielding values of ~36 nm for ZrO_2, ~22 nm for FeO, and ~50 nm for the ZrO_2–FeO@N-rGO nanocomposite. These results confirm nanoscale dimensions, with smaller FeO particles and a slightly larger composite size due to incorporation onto the graphene matrix. A higher surface area promotes stronger interaction between the nanocomposite and microbial cells, thereby enhancing antimicrobial activity. Moreover, the graphene support can facilitate electron transfer processes that further contribute to oxidative stress in microorganisms (Khan *et al.* 2025).

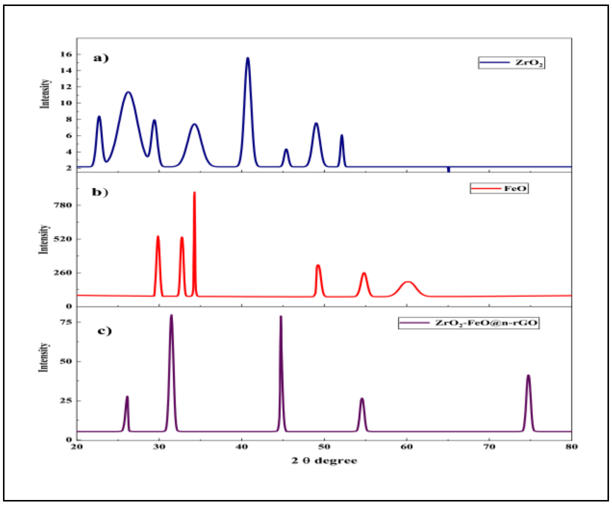

Fig. 8: X-ray diffraction patterns of (a) ZrO_2, (b) FeO and (c) ZrO_2-FeO@N-rGO nanocomposite

3.5 Energy Dispersive X-ray Analysis

EDX spectrum of the synthesized ZrO_2 nanoparticles (Figure 9a) exhibits strong and well-defined signals corresponding to zirconium (Zr) and oxygen (O), confirming the successful formation of zirconium oxide with high elemental purity. The absence of additional metallic peaks indicates that no significant impurities were introduced during synthesis. Similar elemental profiles have been reported for chemically synthesized ZrO_2 nanoparticles, where dominant Zr and O signals validate phase purity and stoichiometric oxide formation (Soltanpour *et al.* 2024).

The EDX spectrum of FeO nanoparticles (Figure 9b) shows intense peaks corresponding to iron (Fe) and oxygen (O), confirming the formation of iron oxide. Minor signals associated with elements such as carbon (C) and chlorine (Cl) are attributed to residual precursor salts, surface-adsorbed species, or the conductive substrate used for EDX analysis (Usharani *et al.* 2022).

For the ZrO_2–FeO@N-rGO nanocomposite (Figure 9c), carbon is shown as a major component with 23.64 wt% (40.71 at%), confirming the presence of a carbon-rich N-rGO conductive framework. Oxygen is observed at 30.80 wt% (39.81 at%), originating from both the ZrO_2 and FeO crystal lattices as well as residual oxygen-containing functional groups on the graphene surface. The detection of nitrogen at 6.12 wt% (5.50 at%) provides clear evidence of successful nitrogen doping, which is known to enhance electrical conductivity and interfacial charge-transfer characteristics. Table 2 shows that iron (18.74 wt%, 6.94 at%) and zirconium (13.38 wt%, 3.03 at%) confirm the effective incorporation of FeO and ZrO_2 phases within the hybrid structure (Potbhare *et al.* 2024). EDAX analysis confirms the presence of iron as the primary constituent with zirconium incorporated in a lower atomic percentage, indicating the formation of a Zr-doped Fe-based nanostructure. Minor contributions from Cl, Si, and Co are attributed to trace precursor residues or instrumental background effects.

Table 2. EDAX elemental composition of the synthesized ZrO_2–FeO@N-rGO nanocomposite confirming the presence of zirconium and iron elements

Element	Weight %	Atomic %	Error %	Net Int.	R	A	F
Fe	18.74	6.94	5.95	124.01	0.9633	0.9832	1.0502
Zr	13.38	3.03	7.70	187.09	0.9235	0.7798	1.0040

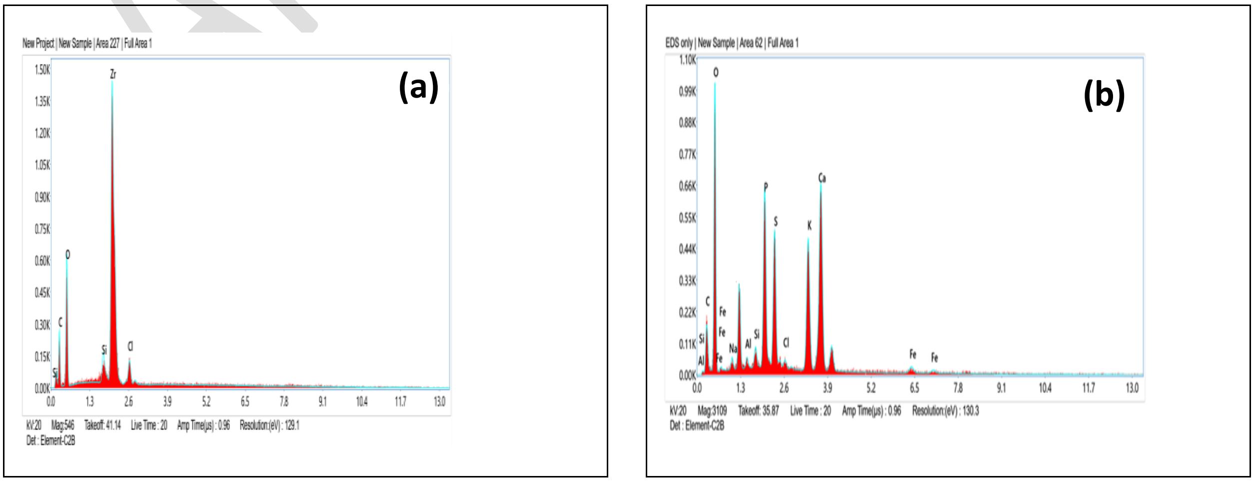

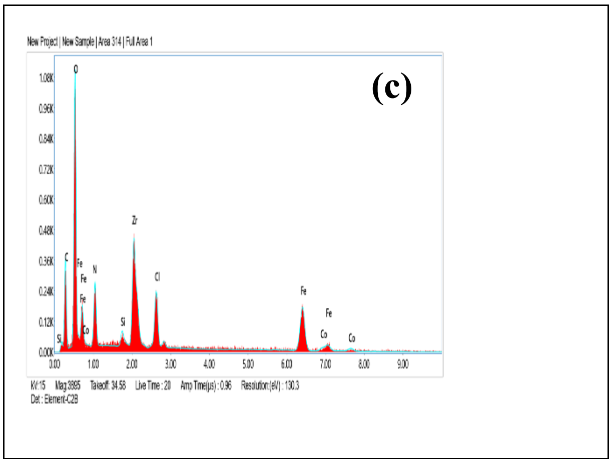

Fig. 9: EDAX spectra of a) ZrO_2, b) FeO and c) ZrO2-FeO@N-rGO nanocomposite

3.6 Dynamic Light Scattering Analysis

Figure 10 illustrates the DLS intensity distributions of ZrO_2 nanoparticles, FeO nanoparticles, and the ZrO_2–FeO@N-rGO nanocomposite. The ZrO_2 nanoparticles (Figure 9a) exhibit a relatively narrow hydrodynamic size distribution in the range of approximately 80–120 nm, indicating good dispersion stability in an aqueous medium. Nanoparticles within this size range are generally considered suitable for biological applications because they provide sufficient surface area for interaction with microbial cells.

In contrast, FeO nanoparticles (Figure 10b) show a broader size distribution centered around 100–180 nm, which may arise from partial agglomeration due to magnetic interactions between iron oxide particles. Such aggregation can sometimes reduce the effective surface area available for biological interaction.

The Z-average hydrodynamic diameter of ZrO_2–FeO@N-rGO was 208.2 nm with a PDI of 0.278. The particle size, compared to individual oxides, is attributed to the anchoring of ZrO_2 and FeO nanoparticles onto the N-rGO sheets and the formation of a surrounding solvation layer. The nanocomposite demonstrates improved dispersion stability due to the presence of graphene sheets, which prevent severe nanoparticle aggregation (Tajik *et al.* 2022; Imran *et al.* 2021).

Additionally, well-dispersed nanoparticles provide more accessible active sites for redox reactions and ROS generation, which are crucial for antimicrobial and antioxidant mechanisms. Similar improvements in colloidal stability and biological performance have been reported for graphene-based metal oxide nanocomposites (Bayzidi and Zeynizadeh, 2022; Tran *et al.* 2022)

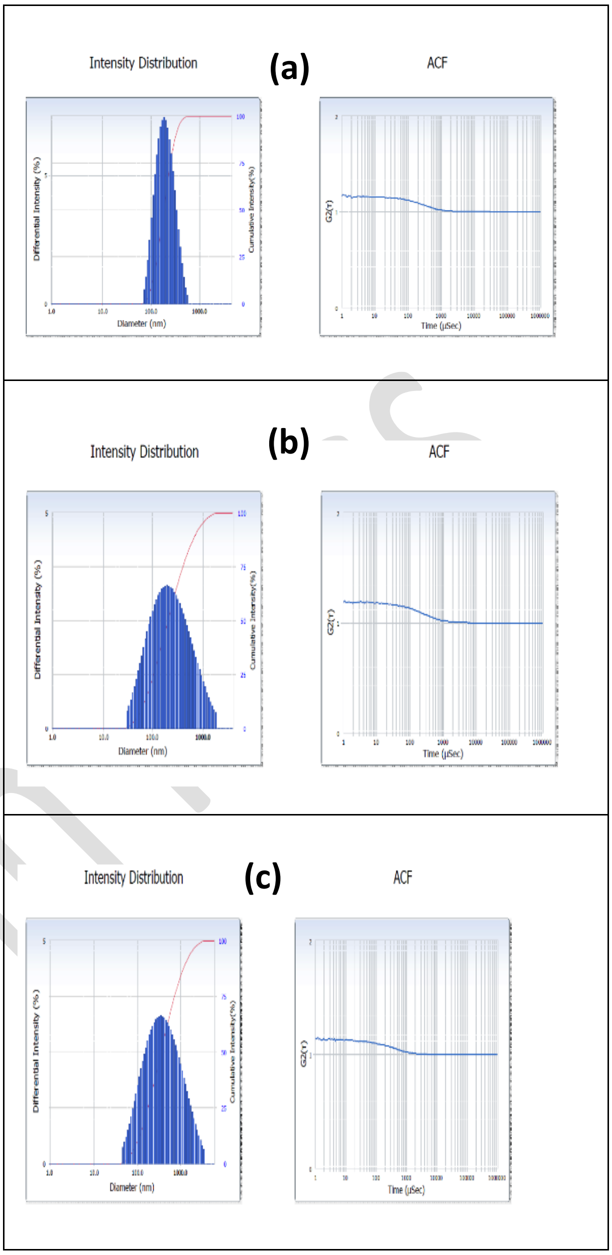

Fig. 10: Dynamic light scattering (DLS) particle size distribution of (a) ZrO_2, (b) FeO and (c) ZrO_2-FeO@N-rGO nanocomposite

3.7 X-ray Photoelectron Spectroscopy

Figure 11 presents the XPS survey spectrum of the ZrO_2–FeO@N-rGO nanocomposite, providing detailed insight into its elemental composition and surface chemical states. The wide-scan spectrum confirms the presence of zirconium (Zr), iron (Fe), carbon (C), oxygen (O), and nitrogen (N), verifying the successful integration of metal oxides within the nitrogen-doped reduced graphene oxide framework (Almars *et al.* 2025).

Strong C 1s and O 1s signals correspond to the carbon framework of N-rGO and oxygen atoms present in both metal oxides and residual surface functional groups. The presence of the N 1s peak confirms the successful nitrogen doping of the graphene lattice. Nitrogen doping is known to modify the electronic structure of graphene, improving its electrical conductivity and electron transfer capability, which can enhance catalytic activity and promote reactive oxygen species generation during biological interactions (Selim *et al.* 2025).

Characteristic Zr 3d peaks confirm the presence of zirconium in its oxidized state, consistent with ZrO_2 formation. Zirconium oxide contributes to improved chemical stability and surface interaction properties, which support the structural integrity of the nanocomposite in biological environments. Meanwhile, the Fe 2p spectrum indicates the presence of mixed Fe^{2+}/Fe^{3+} oxidation states, suggesting the coexistence of different iron oxide species. These nitrogen-doped sites improve electron transfer capability and catalytic activity, which contributes to both ROS generation and efficient radical scavenging in antioxidant assays (Aldahasi and Mohammed, 2025; Jenila *et al.* 2025). Weak Na 1s and Si 2p signals are attributed to trace contamination or substrate effects commonly observed in XPS measurements. Overall, the XPS analysis confirms the successful chemical integration of ZrO_2 and FeO nanoparticles within the N-rGO matrix. The combination of conductive graphene support, redox-active iron species, and chemically stable zirconia is expected to synergistically enhance the biological performance of the hybrid nanocomposite (Khan *et al.* 2025; SefidSiahbandi *et al.* 2025).

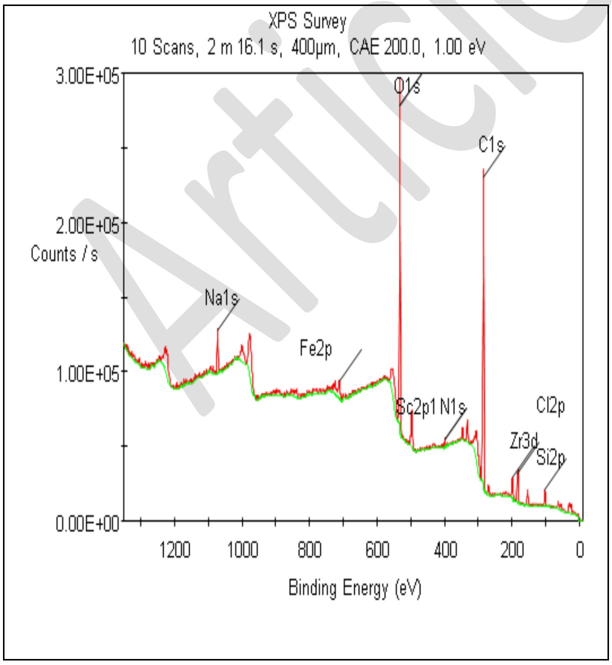

Fig. 11: X-ray photoelectron spectroscopy (XPS) survey spectrum of the ZrO_2-FeO@N-rGO nanocomposite

3.8 Antimicrobial Activity

The antimicrobial activity of the ZrO_2–FeO@N-rGO nanocomposite was evaluated against selected Gram-positive and Gram-negative bacterial strains and fungal species using the agar diffusion method. The results demonstrate a concentration-dependent increase in the zone of inhibition, confirming the effective antimicrobial potential of the nanocomposite in figure 12a (Madhavi *et al.* 2022). Among the tested bacteria, *Proteus vulgaris* exhibited the highest susceptibility, with larger inhibition zones observed at higher concentrations, indicating strong interaction of the nanocomposite with the bacterial cell membrane (Kaliyaperumal *et al.* 2025c). The notable activity against *Actinomyces israelii* further suggests the effectiveness of the nanocomposite against Gram-positive organisms, likely due to enhanced penetration and disruption of the peptidoglycan layer.

Fungal strains also showed significant sensitivity toward the nanocomposite. *Candida albicans* displayed consistent inhibition across concentrations, reflecting effective antifungal action, while *Trichoderma* showed moderate activity with reduced inhibition at lower concentrations, indicating species-dependent susceptibility in Figure 12b. The enhanced antimicrobial performance of the ZrO_2–FeO@N-rGO nanocomposite can be attributed to the synergistic effects of ZrO_2 and FeO nanoparticles integrated within the N-rGO (Shukla *et al.* 2025). The graphene support improves nanoparticle dispersion and surface contact, while nitrogen doping enhances electron transfer and reactive oxygen species (ROS) generation. These mechanisms collectively lead to membrane damage, protein denaturation, and oxidative stress in microbial cells, resulting in growth inhibition. *Proteus vulgaris* and *Actinomyces israelii* were selected due to their clinical relevance in urinary tract and chronic granulomatous infections, respectively, making them suitable models for evaluating the antimicrobial efficacy of the synthesized nanomaterial. Overall, the results confirm that the ZrO_2–FeO@N-rGO nanocomposite exhibits broad-spectrum antimicrobial activity in Table 3 and holds promise for biomedical and environmental applications (Kichukova *et al.* 2022). The antimicrobial activity observed in this study is slightly higher than previously reported values for Fe-based nanocomposites. This enhancement may be attributed to the presence of nitrogen-doped graphene sheets, which improve electron transfer and promote stronger nanoparticle–microbe interactions. The enhanced antimicrobial activity of the ZrO_2–FeO@N-rGO nanocomposite may be attributed to the synergistic interaction between zirconium oxide and iron oxide nanoparticles supported on the conductive N-rGO framework, which facilitates reactive oxygen species (ROS) generation and membrane disruption in microbial cells.

Table 3. Antimicrobial activity of ZrO_2–FeO@N-rGO nanocomposite against selected bacterial and fungal strains measured by agar well diffusion method. Values represent the mean ± standard deviation (SD) of three independent experiments (n = 3); statistical significance was determined using one-way ANOVA with GraphPad Prism 6.0 software (GraphPad Software, USA) ($p < 0.05$). PC = positive control

S.NO	Name of the Test Organism	Zone of Inhibition (mm) Mean ± SD				
		500 µg/ml	250 µg/ml	100 µg/ml	50 µg/ml	PC
A	*A. israelii*	18.25±0.35	17.6±0.14	14.35±0.21	14.1±0.14	17.6±0.14
	P.vulgaris	20.6±0.14	14.95±0.35	12.25±0.35	10.95±0.35	18.75±1.06
B	*Candida albicans*	17.1±0.56	16.7±0.35	14.85±0.21	13.95±0.35	14.45±0.28
	Trichoderma	14.95±0.35	12.85±0.21	12.6±0.14	0	17.6±0.14

SD – Standard Deviation, *Significance - p< 0.05

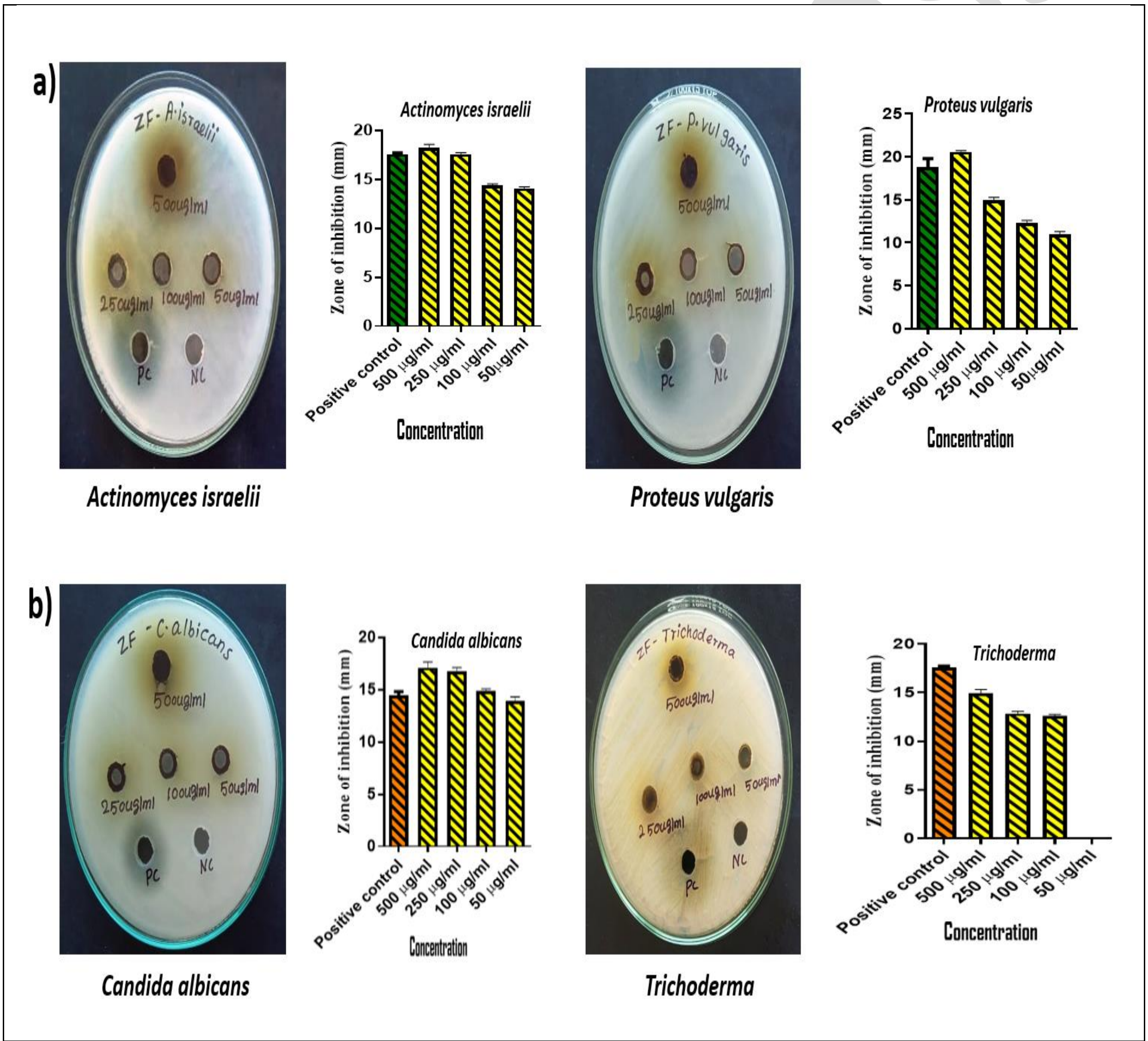

Fig. 12: Antimicrobial activity of ZrO_2–FeO@N-rGO nanocomposite: (a) antibacterial activity and percentage inhibition against *Actinomyces israelii* and *Proteus vulgaris* evaluated using the agar well diffusion method, and (b) antifungal activity and percentage inhibition against *Candida albicans* and *Trichoderma*, demonstrating concentration-dependent inhibitory effects

3.9 Anti-oxidant Activity

3.9.1 DPPH Radical Scavenging Assay

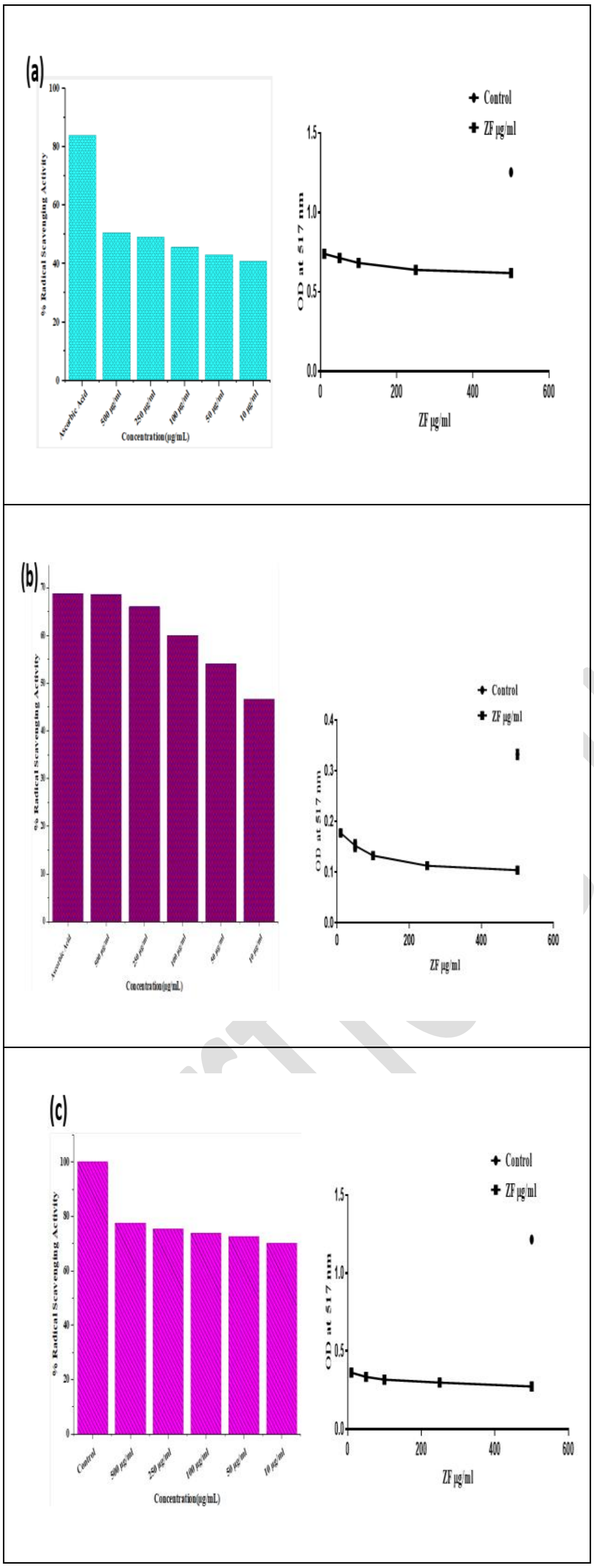

Fig. 13: Antioxidant activity of ZrO_2–FeO@N-rGO nanocomposite at different concentrations: (a) DPPH radical scavenging activity and corresponding absorbance at 517 nm, (b) hydrogen peroxide scavenging activity and absorbance variation, and (c) nitric oxide radical scavenging activity and corresponding absorbance changes, demonstrating concentration-dependent antioxidant behavior. Error bars represent standard deviation (SD) from three independent experiments (n = 3)

The antioxidant potential of the ZrO_2–FeO@N-rGO nanocomposite was assessed using the DPPH radical scavenging assay in Figure 13a. A concentration-dependent decrease in absorbance at 517 nm was observed, indicating effective neutralization of DPPH radicals. The nanocomposite exhibited a maximum inhibition of 50.7% at 500 µg/mL, while lower concentrations showed gradually reduced activity. The calculated IC_{50} value of 101.9 µg/mL confirms moderate yet significant antioxidant efficiency, as shown in Table 4. The high regression coefficient (R^2 = 0.9765) demonstrates good reliability of the dose–response relationship. The observed activity is attributed to synergistic effects between redox-active FeO, surface defect-rich ZrO_2, and electron-donating nitrogen-doped reduced graphene oxide, which together facilitate efficient electron transfer to DPPH radicals. Similar enhancement in antioxidant behavior has been reported for metal oxide–graphene hybrid nanomaterials (Kichukova *et al.* 2022).

Table 4. DPPH radical scavenging activity of ZrO_2–FeO@N-rGO nanocomposite at different concentration values represents triplicate measurements with calculated mean percentage inhibition; the IC_{50} value indicates the concentration required to inhibit 50% of DPPH radicals

S. No.	Tested Sample Concentration (µg/ml)	Percentage of Inhibition (in Triplicates)			Mean Value (%)
1.	Ascorbic acid	84.685	84.264	83.807	84.252
2.	500 µg/ml	51.130	50.625	50.465	50.740
3.	250 µg/ml	49.522	49.123	48.804	49.149
4.	100 µg/ml	46.411	45.534	45.056	45.667
5.	50 µg/ml	44.099	43.222	42.185	43.169
6.	10 µg/ml	41.627	40.909	40.510	41.015
IC_{50} Value of ZrO_2-FeO@N-rGO					101.9 µg/ml

3.9.2 Hydrogen Peroxide Scavenging Assay

H_2O_2 scavenging activity of the ZrO_2–FeO@N-rGO nanocomposite was evaluated by monitoring the decrease in absorbance at 230 nm, as shown in Figure 13b. The nanocomposite exhibited a clear concentration-dependent scavenging behavior, with inhibition increasing from 46.59% at 10 µg/mL to 68.64% at 500 µg/mL, which is comparable to the standard antioxidant ascorbic acid (68.68%) shown in Table 5. The calculated IC_{50} value of 75.59 µg/mL indicates effective scavenging efficiency against H_2O_2 radicals. The strong correlation coefficient ($R^2 = 0.9666$) confirms the reliability of the dose–response relationship. The enhanced antioxidant performance is attributed to the synergistic interaction between redox-active FeO, surface oxygen vacancies in ZrO_2, and the electron-rich nitrogen-doped reduced graphene oxide matrix, which collectively facilitate efficient electron donation and decomposition of hydrogen peroxide into non-toxic species. Similar behavior has been reported for metal oxide–graphene hybrid nanostructures, where interfacial charge transfer significantly improves reactive oxygen species scavenging ability (Le *et al.* 2022).

Table 5. H_2O_2 radical scavenging activity of ZrO_2–FeO@N-rGO nanocomposite at different concentrations, values represent triplicate measurements with calculated mean inhibition percentage

S. No.	Tested Sample Concentration (µg/ml)	Percentage of Inhibition (in Triplicates)			Mean Value
1.	Ascorbic acid	67.898	67.614	70.541	68.684
2.	500 µg/ml	69.339	68.738	67.836	68.638
3.	250 µg/ml	66.934	66.333	64.830	66.032
4.	100 µg/ml	61.223	59.720	59.119	60.020
5.	50 µg/ml	56.714	54.910	50.702	54.109
6.	10 µg/ml	48.297	46.193	45.291	46.594
	IC_{50} Value of ZrO_2-FeO@N-rGO				75.59 µg/ml

3.9.3 Nitric Oxide Radical Scavenging Assay

The nitric oxide radical scavenging activity of the ZrO_2–FeO@N-rGO nanocomposite was assessed by measuring the reduction in absorbance at 540 nm in Figure 13c. The nanocomposite demonstrated a clear dose-dependent inhibition of nitric oxide radicals, with percentage inhibition increasing from 70.21% at 10 µg/mL to 77.56% at 500 µg/mL, as shown in Table 6. The calculated IC_{50} value of 98.06 µg/mL indicates moderate to strong NO scavenging efficiency. The good linearity of the dose–response curve ($R^2 = 0.9134$) confirms the reliability of the antioxidant response. The observed activity can be attributed to the synergistic effects of redox-active FeO, oxygen-rich ZrO_2 surfaces, and the electron-donating N-rGO matrix, which collectively facilitate the neutralization of nitric oxide radicals. Similar enhancement of NO scavenging has been reported for metal oxide–graphene nanocomposites, where interfacial charge transfer and surface functional groups play a crucial role in suppressing reactive nitrogen species (Sarvalkar *et al.* 2025; Nivetha *et al.* 2026; Kathirvel *et al.* 2025; Kaliyaperumal *et al.* 2025d).

Table 6. Nitric oxide radical scavenging activity of ZrO_2–FeO@N-rGO nanocomposite at different concentrations, Values represent triplicate measurements with calculated mean inhibition percentage

S. No.	Tested Sample Concentration (µg/ml)	Percentage of Inhibition (in Triplicate)			Mean Value (%)
1.	Control	100	100	100	100
2.	500 µg/ml	78.4421	77.2078	77.04327	77.5644
3.	250 µg/ml	76.7964	75.0685	74.65709	75.5073
4.	100 µg/ml	74.4102	74.1634	73.17601	73.916
5.	50 µg/ml	72.7646	72.2709	72.43547	72.4903
6.	10 µg/ml	71.119	70.1316	69.39103	70.2139
	IC_{50} Value of ZrO_2-FeO@N-rGO				98.06 µg/ml

4. CONCLUSIONS

The ZrO_2–FeO@N-rGO nanocomposite was successfully synthesized and systematically characterized. UV–Visible analysis showed absorption maxima at 202 nm for ZrO_2, 247 nm for FeO, and 203 nm for ZrO_2–FeO@N-rGO, respectively. FT-IR analysis confirmed the characteristic O–H, C=C, and metal–oxygen vibrations, with prominent bands at 3434–3453, 1634–1638, 1540–1560, 711, and 688 cm^{-1}, while the composite exhibited a shifted metal–oxygen band at approximately 661 cm^{-1}, supporting interfacial interactions within the hybrid structure. XRD verified the crystalline phases of ZrO_2 and iron oxide. SEM and TEM showed well-dispersed ZrO_2 and FeO nanoparticles anchored onto wrinkled N-rGO sheets with distinct lattice fringes and polycrystalline SAED patterns. The Z-average hydrodynamic diameter of ZrO_2–FeO@N-rGO was 208.2 nm with a PDI of 0.278. EDAX confirmed Fe and Zr contents of 18.74 wt% and 13.38 wt%, respectively, corresponding to 6.94 and 3.03 atomic %. XPS further confirmed the presence of Zr, Fe, C, O, and N, with Zr^{4+} and mixed Fe^{2+}/Fe^{3+} surface states.

The biological evaluation demonstrated concentration-dependent antioxidant and antimicrobial activities. At 500 µg/mL, the nanocomposite showed 50.7% DPPH, 68.64% H_2O_2, and 77.56% nitric oxide scavenging, with IC_{50} values of 101.9, 75.59, and 98.06 µg/mL, respectively. The H_2O_2 scavenging activity was comparable to ascorbic acid (68.68%). Antimicrobial studies showed maximum inhibition zones of 20.60 ± 0.14 mm against *P. vulgaris*, 18.25 ± 0.35 mm against *A. israelii*, 17.10 ± 0.56 mm against *Candida albicans*, and 14.95 ± 0.35 mm against *Trichoderma* sp. at 500 µg/mL.

Overall, the obtained structural, morphological, optical, and biological results confirm the successful formation of ZrO_2–FeO@N-rGO as a multifunctional nanocomposite with appreciable antioxidant and antimicrobial properties. The combination of nanoscale structure, effective metal oxide incorporation, and biological activity highlights its potential for further exploration in biomedical and environmental applications.

DECLARATION OF AI USE

The authors declare that the Perplexity AI tool was used solely for language editing, grammar correction, and improvement of clarity and readability of the manuscript. The tool did not contribute to the study design, data analysis, interpretation of results, or the generation of scientific content. The authors take full responsibility for the content of this manuscript.

AUTHOR CONTRIBUTIONS

S. Nivetha contributed to the methodology and was responsible for writing the original draft and subsequent review and editing of the manuscript. Dr. J. Rosaline Vimala contributed to conceptualization, project administration, provision of resources, supervision of the research work, and funding acquisition. A. Devadharshini Amala contributed to data curation, visualization, and software-related activities. Dr. A. Agila contributed to the investigation. Dr. A. Anitha Immaculate was responsible for validation of the research findings. Dr. Chinnappan Baskar contributed to formal analysis and validation. All authors reviewed the manuscript, participated in the revision process, and approved the final version of the manuscript.

FUNDING

This research received no specific grant from any funding agency in the public, commercial, or not-for-profit sectors.

CONFLICTS OF INTEREST

The authors declare that there is no conflict of interest.

COPYRIGHT

REFERENCES

Agarwal, V. and Zetterlund, P. B., Strategies for reduction of graphene oxide—A comprehensive review, *Chem. Eng. J.*, 405, 127018 (2021). https://doi.org/10.1016/j.cej.2020.127018

Águila-Martínez, I., Pérez-Tavares, J. A., González-Aguiñaga, E., Cardoso-Avila, P. E., Pérez Ladrón de Guevara, H. and Patakfalvi, R., Synthesis and application of Fe_3O_4-ZrO_2 magnetic nanoparticles for fluoride adsorption from water, *Inorg.*, 13(7), 248 (2025). https://doi.org/10.3390/inorganics13070248

Al-Ansari, S. H., Gomaa, H., Abdel-Rahim, R. D., Ali, G. A. M. and Adham, N. M., Recycled gold-reduced graphene oxide nanocomposite for efficient adsorption and photocatalytic degradation of crystal violet, *Sci. Rep.*, 14(1), 54580 (2024). https://doi.org/10.1038/s41598-024-54580-1

Al-Gaashani, R., Pasha, M., Jabbar, K. A., Shetty, A. R., Baqiah, H., Mansour, S., Viktor, K. and Jenny, L., Antimicrobial activity of ZnO-Ag-MWCNTs nanocomposites prepared by a simple impregnation-calcination method, *Sci. Rep.*, 13(1), 21418 (2023). https://doi.org/10.1038/s41598-023-48831-w

Aldahasi, R. M. and Mohammed, A. E., Bimetallic nanocomposite produced from *Acacia tortilis* subsp. *raddiana* for the mitigation fungal pathogens in tomatoes, *Sci. Rep.*, 15(1), 41592 (2025). https://doi.org/10.1038/s41598-025-25419-0

Almars, A. I., Green-synthesized $MnFe_2O_4$/GO nanocomposites: structural characterization, cytotoxicity, and potential for targeted cervical cancer therapy, *Cancer Cell Int.*, 25(1), 355 (2025). https://doi.org/10.1186/s12935-025-03953-1

Anjaneyulu, R. B., Mohan, B. S., Naidu, G. P. and Muralikrishna, R., ZrO_2/Fe_2O_3/RGO nanocomposite: Good photocatalyst for dye degradation, *Phys. E Low-Dimens. Syst. Nanostruct.*, 108, 105-111 (2019). https://doi.org/10.1016/j.physe.2018.12.007

Arayesh, M. A., Kianfar, A. H. and Mohammadnezhad, G., Synthesis of Fe_3O_4/ZrO_2/ZnO nanoparticles for enhancing visible light photocatalytic and antibacterial activity, *J. Taiwan Inst. Chem. Eng.*, 153, 105213 (2023). https://doi.org/10.1016/j.jtice.2023.105213

Bayzidi, M. and Zeynizadeh, B., A uniformly anchored zirconocene complex on magnetic reduced graphene oxide (rGO@$Fe_3O_4/ZrCp_2Cl_x$, x = 0, 1, 2) as a novel and reusable nanocatalyst for synthesis of N-arylacetamides and reductive-acetylation of nitroarenes, *RSC Adv.*, 12(24), 15020-15037 (2022). https://doi.org/10.1039/D2RA02293A

Devendran, N. and Lakshmi, T. S., Investigation on the physical and mechanical properties of banana/ramie hybrid composites reinforced with graphene oxide nanoparticles, *J. Environ. Nanotechnol.*, 14(3), 193-204 (2025). https://doi.org/10.13074/jent.2025.09.2531639

Elshypany, R., Selim, H., Zakaria, K., Moustafa, A. H., Sadeek, S. A., Sharaa, S. I., Patrice, R. and Amr, A. N., Elaboration of Fe_3O_4/ZnO nanocomposite with highly performance photocatalytic activity for degradation methylene blue under visible light irradiation, *Environ. Technol. Innov.*, 23, 101710 (2021). https://doi.org/10.1016/j.eti.2021.101710

Gautam, A., Dabral, H., Singh, A., Tyagi, S., Tyagi, N., Srivastava, D. and Anu, S., Graphene-based metal/metal oxide nanocomposites as potential antibacterial agents: A mini-review, *Biomater. Sci.*, 12(18), 4630-4649 (2024). https://doi.org/10.1039/d4bm00796d

Gayathri, V. and Balan, R., Synthesis and Characterization of Pure Zirconium Oxide (ZrO_2) Nanoparticles by Conventional Precipitation Method, *J. Environ. Nanotechnol.*, 10(4), 19–21 (2021). https://doi.org/10.13074/jent.2021.12.214447

Hussein, S. A., Taha, G. M., Adam, F. A. and Marwa, M. A., Three different methods for ZnO-RGO nanocomposite synthesis and its adsorption capacity for methylene blue dye removal, *BMC Chem.*, 19(1), 81 (2025). https://doi.org/10.1186/s13065-025-01381-w

Imran, M., Alam, M. M., Hussain, S., Ali, M. A., Shkir, M., Mohammad, A., Tansir, A., Ajeet, K. and Kashif, I., Highly photocatalytic active r-GO/Fe_3O_4 nanocomposites development for enhanced photocatalysis application: A facile low-cost preparation and characterization, *Ceram. Int.*, 47(22), 31973-31982 (2021). https://doi.org/10.1016/j.ceramint.2021.08.083

Jenila, T. J., Infancy, W. T., Rathikha, R., Vinosha, P. A., Ayyar, M., Ramasamy, S., Maruthasalamoorthy, S., Navamathavan, R., Belina, X., Abdullah, A. M. S., Hala, A. D. H., Magda, A. H., Balachandran, R. and Khalid, M. H., Unraveling the role of MXene ($Ti_3C_2T_x$) integrated Cu-doped WO_3 nanocomposites via co-precipitation technique for enhanced supercapacitor performance, *Sci. Rep.*, 15(1), 25007 (2025). https://doi.org/10.1038/s41598-025-10174-z

Kaliyaperumal, R., Nagaraj, K., Badgujar, N. P., Kasilingam, T., Poovan, V. and Kumaravel, T., Enhanced antimicrobial activity of bismuth oxide doped copper oxide nanocomposites synthesized via co-precipitation: Influence of composition and morphology, *BioNanoSci.*, 15(3), 399 (2025a). https://doi.org/10.1007/s12668-025-02019-w

Kaliyaperumal, R., Nagaraj, K., Kasilingam, T., Kumaravel, T. and Gokulan, R., Synthesis, characterization, and biological evaluation of PbO/g-C_3N_4 nanocomposite: A multifunctional material for antimicrobial, antioxidant, anti-inflammatory, and cytotoxic applications, *BioNanoSci.*, 15(3), 451 (2025b). https://doi.org/10.1007/s12668-025-02082-3

Kaliyaperumal, R., Suresh, S., Rajaraman, D., Shah, M., Wahid, J. B. A., Kasilingam, T., Tharini, K., Ramakrishnan, J. and Nagaraj, K., CuO@CdO/MgO nanocomposites: Composition-driven photocatalysis, energy storage, and biocompatibility, *Chem. Eng. Technol.*, 48(12), e70142 (2025c). https://doi.org/10.1002/ceat.70142

Kaliyaperumal, R., Nagaraj, K., Wadaan, M. A., Poovan, V. K., Ghodake, G. S., Badgujar, N. P. and Kumaravel, T., Development and antimicrobial evaluation of tin oxide (SnO_2) nanoparticles stabilized with corn cob ash extract for biomedical applications, *Biomed. Mater. Dev.*, 4, 2379-2388(2025d). https://doi.org/10.1007/s44174-025-00212-5

Kathirvel, A., Srinivasan, R., Harini, S., Ranjith, N., Kumar, G. S., Lalithambigai, K., Raji, A., Habila, M. A., Ahmed, A. M. and Yun, H. K., Eco-friendly synthesis of zirconium dioxide nanoparticles from *Toddalia asiatica*: Applications in dye degradation, antioxidant and antibacterial activity, *Nanomater.*, 15(2), 84 (2025). https://doi.org/10.3390/nano15020084

Khan, Z. U., Jiang, J. and Atif, M., Nanostructured bimetallic oxide/graphene nanocomposites for next-generation high-performance energy storage, *Int. J. Environ. Res.*, 19(6), 223 (2025). https://doi.org/10.1007/s41742-025-00895-4

Kichukova, D., Spassova, I., Kostadinova, A., Staneva, A. and Kovacheva, D., Facile synthesized Cu-RGO and Ag-RGO nanocomposites with potential biomedical applications, *Nanomater.*, 12(12), 2096 (2022). https://doi.org/10.3390/nano12122096

Korde, S., Tandekar, S., Jeyaseelan, C., Saravanan, D. and Jugade, R., Mesoporous magnetic chitosan-zirconia-iron oxide nanocomposite for adsorptive removal of Cr(VI) ions, *Mater. Lett.*, 311, 131513 (2022). https://doi.org/10.1016/j.matlet.2021.131513

Kumar, R. S., Yuvaperiyasamy, M., Sathish, R., Miniappan, P. K. and Arivalagan, P., Impact loading on polymer nanocomposites—A comprehensive review, *J. Environ. Nanotechnol.*, 13(3), 424-434 (2024). https://doi.org/10.13074/jent.2024.09.243821

Le, T. D. H., Tuan, H. N. A., Trinh, K. S. and Van, K. T., Enhanced antibacterial property of zinc oxide nanoparticles by incorporation of graphene oxide, *J. Sol-Gel Sci. Technol.*, 104(1), 246-257 (2022). https://doi.org/10.1007/s10971-022-05923-9

Lee, M., Han, S. I., Kim, C., Velumani, S., Han, A., Kassiba, A. H. and Castaneda, H., ZrO_2/ZnO/TiO_2 nanocomposite coatings on stainless steel for improved corrosion resistance, biocompatibility, and antimicrobial activity, *ACS Appl. Mater. Interf.*, 14(11), 13801-13811 (2022). https://doi.org/10.1021/acsami.1c19498

Liu, Y., Meng, L., Han, K. and Sun, S., Synthesis of nano-zirconium-iron oxide supported by activated carbon composite for the removal of Sb(V) in aqueous solution, *RSC Adv.*, 11(49), 31131-31141 (2021). https://doi.org/10.1039/D1RA06117H

Madhavi, Kumar, M., Ansari, J. R., Kumar, V., Nagar, S. and Sharma, A., Fe_3O_4 coated SiO_2 magnetic nanoparticles for enhanced antibacterial activity and electrochemical sensing, *Metals*, 12(12), 2145 (2022). https://doi.org/10.3390/met12122145

Madhuranga, H. D. T. and Samarakoon, D. N. A. W., Advancing in vitro antioxidant activity assessment: A comprehensive methodological review and improved approaches for DPPH, FRAP, and H_2O_2 assays, *J. Nat. Ayurved. Med.*, 7(4), 1-7 (2023). https://doi.org/10.23880/jonam-16000431

Mohan, C. N., Ayyadurai, V., Nagaraj, K., Kumar, P. V., Raja, K., Suganthi, P., Muthukumar, C. and Stalin, A., Green synthesis of copper hydroxide nanorods using *Solanum pubescens* leaf extracts: A promising approach for antimicrobial, antioxidant, and anticancer applications, *3 Biotech*, 15(9), 277 (2025). https://doi.org/10.1007/s13205-025-04404-4

Munteanu, I. G. and Apetrei, C., Analytical methods used in determining antioxidant activity: A review, *Int. J. Mol. Sci.*, 22(7), 3380 (2021). https://doi.org/10.3390/ijms22073380

Mustafa, Y. F., Modern developments in the application and function of metal/metal oxide nanocomposite-based antibacterial agents, *BioNanoSci.*, 13(2), 840-852 (2023). https://doi.org/10.1007/s12668-023-01100-6

Mylarappa, M., Selvam, C., Harisha, K. S., Kumar, P. S. G., Krishnamurthy, G. and kalasad, M. N., Reduced graphene oxide loaded La_2O_3 nanocomposite for dye degradation and antioxidant studies, *Res. Surf. Interf.*, 14, 100202 (2024). https://doi.org/10.1016/j.rsurfi.2024.100202

Nagaraj, K., Kaliyaperumal, R., Poovan, V. K., Al-Sadoon, M. K., Kasilingam, T. and Tharini, K., Zirconium-doped zinc nanocomposites (ZDZN): Preparation, characterization, and evaluation of antibacterial activity, *J. Indian Chem. Soc.*, 101(11), 101386 (2024). https://doi.org/10.1016/j.jics.2024.101386

Nanda, S. S. and Yi, D. K., Recent advances in synergistic effect of nanoparticles and its biomedical application, *Int. J. Mol. Sci.*, 25(6), 3266 (2024). https://doi.org/10.3390/ijms25063266

Nivetha, S., Vimala, J. R., Amala, A. D. and Immaculate, A. A., Rutin-mediated synthesis of Zr-Mg@N-rGO nanocomposites with potent antioxidant and antimicrobial activities, *Asian J. Chem.*, 38(2), 334-342 (2026). https://doi.org/10.14233/ajchem.2026.34942

Noormohamadi, A., Homayoonfal, M., Mehrnia, M. R. and Davar, F., Synergistic effect of concurrent presence of zirconium oxide and iron oxide in the form of core-shell nanoparticles on the performance of Fe_3O_4@ZrO_2/PAN nanocomposite membrane, *Ceram. Int.*, 43(18), 17174-17185 (2017). https://doi.org/10.1016/j.ceramint.2017.09.142

Potbhare, A. K., Aziz, S. K. T., Ayyub, M. M., Kahate, A., Madankar, R., Wankar, S., Dutta, A., Abdala, A., Mohmood, S. H., Adhikari, R. and Chaudhary, R. G., Bioinspired graphene-based metal oxide nanocomposites for photocatalytic and electrochemical performances: An updated review, *Nanoscale Adv.*, 6(10), 2539-2568 (2024). https://doi.org/10.1039/D3NA01071F

Rajalakshmi, K., Thangamani, C., Sekar, S., Somaily, H. H., Aadil, M., Alanazi, A. K. and Nagaraj, K., Metallosurfactant-assisted synthesis of Fe-doped NiO nanoclusters with tunable multifunctional properties, *Surf. Interf.*, 78, 108044 (2025). https://doi.org/10.1016/j.surfin.2025.108044

Rane, A. V., Kanny, K., Abitha, V. K. and Thomas, S., Methods for synthesis of nanoparticles and fabrication of nanocomposites, *Synth. Inorg. Nanomater.*, 121-139 (2018). https://doi.org/10.1016/B978-0-08-101975-7.00005-1

Sahoo, A., Acharya, A. N., Jena, P., Moonis, M., Biswal, J. P., Swain, S. and Tripathy, M. C., Zirconium ferrite nanoparticles as smart materials for energy and environmental applications: Fractional-order supercapacitors, reservoirs of F^- ions, and efficient electrocatalysts for water splitting, *Nanoscale Adv.*, 7(20), 6575-6595 (2025). https://doi.org/10.1039/D5NA00578G

Sanjeevarayappa, C., Nagegowda, P., Mylarappa, M., Chandruvasan, S., Sandhya, R. and Prasanna, K. S., Biological and electrochemical sensor detection studies of ZrO_2 wrapped by reduced graphene oxide nanocomposite, *Mater. NanoSci.*, 11(1), 952 (2024).

Sanmugam, A., Sellappan, L. K., Almeer, R., Manoharan, S., Karuppasamy, K., Kathalingam, A., Akram, A., Maiyalagan, T., Vikraman, D. and Kim, H. S., Facile synthesis of reduced graphene oxide-zirconium oxide/zinc oxide nanocomposites for effective antimicrobial and cytotoxic applications, *Surf. Interf.*, 53, 105026 (2024). https://doi.org/10.1016/j.surfin.2024.105026

Sarvalkar, P. D., Jagtap, A. S., Prasad, N. R., Yaul, A. R., Sharma, K. K. K. and Ramteke, A. A., Bio-inspired preparation of Ag NPs, rGO, and Ag/rGO nanocomposites for acoustical, antioxidant, and plant growth regulatory studies, *Sci. Rep.*, 15(1), 3281 (2025). https://doi.org/10.1038/s41598-025-87705-1

SefidSiahbandi, M., Moradi, O. and Akbari-Adergani, B., Synergistic effect of bimetallic based nanocomposites for removal of pharmaceutical compounds in water purification: A review, *ChemSelect*, 10(20), e202405406 (2025). https://doi.org/10.1002/slct.202405406

Selim, S., Almuhayawi, M. S., Saddiq, A. A., Alruhaili, M. H., Saied, E., Sharaf, M. H., Tarabulsi, M. K. and Soad, A. J. K., Synthesis of novel MgO-ZnO nanocomposite using *Pluchea indica* leaf extract and study of their biological activities, *Bioresour. Bioprocess.*, 12(1), 33 (2025). https://doi.org/10.1186/s40643-025-00848-x

Shaba, E. Y., Tijani, J. O., Jacob, J. O., Suleiman, M. A. T. and Mathew, J. T., Preparation, characterization, and adsorptive and antimicrobial properties of Fe_3O_4@SiO_2@ZnO nanocomposite, *Colloids Surf. A Physicochem. Eng. Asp.*, 686, 133190 (2024). https://doi.org/10.1016/j.colsurfa.2024.133190

Sharma, G., Kumar, A., Sharma, S., Naushad, M., Dwivedi, R. P., AlOthman, Z. A. and Mola, G. T., Novel development of nanoparticles to bimetallic nanoparticles and their composites: A review, *J. King Saud Univ. Sci.*, 31(2), 257-269 (2019). https://doi.org/10.1016/j.jksus.2017.06.012

Shukla, S., Gupta, A. R., Shaji, S. K. and Sharma, S., Designing of highly efficient chitosan-based bimetallic Zr-Fe three-dimensional bio-architecture for mitigating fluoride from water, *Biomass Convers. Biorefin.*, 15(7), 10897-10915 (2025). https://doi.org/10.1007/s13399-024-05927-1

Soltanpour, P., Naderali, R. and Mabhouti, K., Comparative study on structural, morphological, and optical properties of MS/Fe_3O_4 nanocomposites and M-doped Fe_3O_4 nanopowders (M = Mn, Zn), *Sci. Rep.*, 14(1), 21287 (2024). https://doi.org/10.1038/s41598-024-72026-6

Stephanie, R., Kim, M. W., Kim, S. H., Kim, J. K., Park, C. Y. and Park, T. J., Recent advances of bimetallic nanomaterials and its nanocomposites for biosensing applications, *TrAC Trends Anal. Chem.*, 135, 116159 (2021). https://doi.org/10.1016/j.trac.2020.116159

Tajik, S., Askari, M. B., Ahmadi, S. A., Nejad, F. G., Dourandish, Z., Razavi, R., Hadi, B. and Antonio, D. B., Electrochemical sensor based on $ZnFe_2O_4$/RGO nanocomposite for ultrasensitive detection of hydrazine in real samples, *Nanomater.*, 12(3), 491 (2022). https://doi.org/10.3390/nano12030491

Thamer, A. A., Jubier, N. J. and Odah, J. F., Synthesis and characterization (ZrO_2:MgO) nanocomposite and assessed biocompatibility in vitro by SBF and MTT assay, *AIP Conf. Proc.*, 2922(1), 040009 (2024). https://doi.org/10.1063/5.0183343

Tran, T. V., Nguyen, D. T. C., Kumar, P. S., Din, A. T. M., Jalil, A. A. and Vo, D. V. N., Green synthesis of ZrO_2 nanoparticles and nanocomposites for biomedical and environmental applications: A review, *Environ. Chem. Lett.*, 20(2), 1309-1331 (2022). https://doi.org/10.1007/s10311-021-01329-3

Usharani, B., Murugadoss, G., Rajesh Kumar, M. and Manivannan, V., Reduced graphene oxide supported ZrO_2-based nanocomposites: Structural and functional evaluation, *Catal.*, 12(10), 1249 (2022). https://doi.org/10.3390/catal12101249

Vengatesan, M. R., Darawsheh, I. F. F., Govindan, B., Alhseinat, E. and Banat, F., Ag-Cu bimetallic nanoparticle decorated graphene nanocomposite as an effective anode material for hybrid capacitive deionization system, *Electrochim. Acta*, 297, 1052-1062 (2019). https://doi.org/10.1016/j.electacta.2018.12.004

Yang, Z., Zheng, X. and Zheng, J., A facile one-step synthesis of Fe_2O_3/nitrogen-doped reduced graphene oxide nanocomposite for enhanced electrochemical determination of dopamine, *J. Alloys Compd.*, 709, 581-587 (2017). https://doi.org/10.1016/j.jallcom.2017.03.201